Accurate electronic free energies of the 3d,4d, and 5d transition metals at high temperatures

Zhang, Xi; Grabowski, Blazej; Freysoldt, Christoph; Kormann, Fritz; Neugebauer, Jörg

DOI
10.1103/PhysRevB.95.165126

Publication date
2017

Document Version
Final published version

Published in
Physical Review B (Condensed Matter and Materials Physics)

Citation (APA)
Zhang, X., Grabowski, B., Freysoldt, C., Kormann, F., & Neugebauer, J. (2017). Accurate electronic free energies of the 3*d*,4*d*, and 5*d* transition metals at high temperatures. *Physical Review B (Condensed Matter and Materials Physics)*, *95*(16), Article 165126. https://doi.org/10.1103/PhysRevB.95.165126

Accurate electronic free energies of the 3*d*, 4*d*, and 5*d* transition metals at high temperatures

Xi Zhang,[1,*] Blazej Grabowski,[1] Fritz Körmann,[1,2] Christoph Freysoldt,[1] and Jörg Neugebauer[1]
[1]*Max-Planck-Institut für Eisenforschung GmbH, D-40237, Düsseldorf, Germany*
[2]*Department of Materials Science and Engineering, Delft University of Technology, Mekelweg 2, 2628 CD Delft, Netherlands*
(Received 30 September 2016; revised manuscript received 13 March 2017; published 19 April 2017)

Free energies of bulk materials are nowadays routinely computed by density functional theory. In particular for metals, electronic excitations can significantly contribute to the free energy. For an ideal static lattice, this contribution can be obtained at low computational cost, e.g., from the electronic density of states derived at $T = 0$ K or by utilizing the Sommerfeld approximation. The error introduced by these approximations at elevated temperatures is rarely known. The error arising from the ideal lattice approximation is likewise unexplored but computationally much more challenging to overcome. In order to shed light on these issues we have computed the electronic free energies for all 3*d*, 4*d*, and 5*d* transition elements on the ideal lattices of the bcc, fcc, and hcp structures using finite-temperature density-functional theory. For a subset of elements we have explored the impact of explicit thermal vibrations on the electronic free energies by using *ab initio* molecular dynamics simulations. We provide an analysis of the observed chemical trends in terms of the electronic density of states and the canonical *d* band model and quantify the errors in the approximate methods. The electronic contribution to the heat capacities and the corresponding errors due to the different approximations are studied as well.

DOI: 10.1103/PhysRevB.95.165126

I. INTRODUCTION

Free energies determine thermodynamic phase stabilities and phase diagrams and are, therefore, a key ingredient to materials design. In the past years extensive efforts have been undertaken to develop *ab initio* methods, mainly based on density-functional theory (DFT), for computing accurate free energies [1–7]. A particular challenge in doing so is the inclusion of all relevant excitation mechanisms up to the melting temperature related to atomic, electronic, and, for magnetic materials, spin degrees of freedom. Neglecting the nonadiabatic coupling between the different degrees of freedom, such an approach can be systematically developed on top of the free energy Born-Oppenheimer approximation [8,9]. Although atomic vibrations (quasiharmonic part) dominate the free energy at elevated temperatures, the neglect or an inaccurate evaluation of seemingly minor contributions (e.g., electronic, magnetic, or anharmonic) can result in falsely predicted phase stabilities or inaccurate phase transition temperatures.

In this work we focus on approaches for computing electronic free energies. For atoms on ideal lattice positions the electronic free energy can be computed rather efficiently. Available approaches are (a) a self-consistent field (SCF) finite temperature DFT calculation, (b) the fixed density of states (DOS) approximation that neglects the implicit temperature dependence of the electronic DOS of the self-consistent formalism, or (c) a further approximation that considers only the effective, temperature independent DOS at the Fermi level [Sommerfeld approximation (SOM)] [10]. These approaches are introduced in detail in Sec. II. The literature survey in Table I reveals that the two approximate methods (DOS and SOM) prevail in actual applications over the SCF method. This is understandable because the latter requires multiple self-consistent cycles to derive the full temperature dependence of the electronic free energy, even if the atoms are restricted to their ideal lattice sites. The other two methods are computationally more appealing because either a single self-consistent calculation (fixed DOS approximation) or even a single value of the DOS at the Fermi level (Sommerfeld approximation) are sufficient. Despite the widespread use of these two approximate methods over the last decades, their actual, quantitative performance is not known.

Besides the fixed DOS and Sommerfeld approximation, a typical implicit assumption is that the atoms are restricted to their ideal $T = 0$ K lattice positions. At high temperatures, however, lattice vibrations become significant and may alter the electronic states and thus the electronic free energy [5]. In order to fully incorporate the impact of lattice vibrations on the electronic free energy, computationally expensive *ab initio* molecular dynamic (AIMD) simulations are required. This fact has drastically limited the number of corresponding studies [28,29], and so far the importance of explicit vibrations remains elusive.

In the present work we address these issues by performing a study of *ab initio* electronic free energies and heat capacities for all 3*d*, 4*d*, and 5*d* transition elements on the ideal lattices of the bcc, fcc, and hcp phases. For a subset of relevant elements and phases we perform explicit AIMD calculations. We provide an analysis of the observed chemical trends in terms of the electronic DOS and the canonical *d* band model [30–32] and quantify the error introduced by the different approximations.

*xizhang@mpie.de

II. THEORY

A. SCF finite temperature DFT approach

The finite temperature extension to DFT was developed by Mermin [33]. Mermin [33] extended the original Hohenberg-Kohn theorem [34] by proving the existence of a functional

TABLE I. Compilation of several previous *ab initio* studies on electronic free energies for ideal lattices, highlighting the employed methodology: SCF=self-consistent field method; DOS=fixed DOS approximation; SOM=Sommerfeld approximation; "x" indicates the used method, whereas "c" means that results by this method were shown for comparison only.

			Method		
Year	Ref.	Material	SCF	DOS	SOM
1986	[11]	Fe		x	
1995	[10]	Ni-V, Pd-V		x	c
1996	[12]	Fe		x	
1996	[13]	Sc, Ti, V, Cr, Y, Zr, Nb, Mo		x	
1998	[14]	Al-Mn-Pd, Al-Re-Pd			x
1998	[15]	Nb_3Sn	x		x
2002	[16]	Ce			x
2004	[17]	Al, Ni, NiAl, Ni_3Al		x	
2005	[18]	Ni-Al		x	
2005	[19]	Ni-Al		x	c
2006	[20]	YB_6			x
2007	[21]	Al, Pb, Cu, Ag, Au, Pd, Pt, Rh, Ir	x		
2007	[22]	Ti			x
2008	[23]	Al, Cu, Ag, Au, Ni, Pt, W, Ti		x	c
2010	[24]	Al, Cu, Ni, Mo, Ta, Ni-Al, Ni_3Al		x	
2011	[25]	Ca	x		
2011	[26]	Model study		x	x
2016	[27]	High entropy alloys			x

of the electronic density which uniquely determines the thermodynamic equilibrium ensemble at finite temperatures. This theorem implies that—given the exact temperature-dependent exchange-correlation functional—the free energy contribution due to the electronic degrees of freedom is exactly determined for a fixed set of atomic coordinates. In practice one is presently restricted to approximations which only implicitly depend on temperature, via the charge density, but which do not include explicit temperature effects [35].

Despite this inherent approximation, finite temperature DFT has been shown to capture a major part of the electronic contribution to the free energy and thus to thermodynamic properties [21,36]. Therefore it can be considered as a highly accurate *ab initio* method. The key quantity in such an approach is the electronic charge density,

$$\rho(\mathbf{r},T) = \sum_i f(\varepsilon_i,T)\,|\phi_i(\mathbf{r})|^2, \tag{1}$$

where $\mathbf{r}$ is a three-dimensional real space vector, T the temperature, and where the sum runs over Kohn-Sham single particle orbitals ϕ_i [37] weighted with Fermi-Dirac occupation numbers,

$$f(\varepsilon_i,T) = \left[\exp\left(\frac{\varepsilon_i-\varepsilon_\mathrm{F}}{k_BT}\right)+1\right]^{-1}, \tag{2}$$

where ε_i is the energy of ϕ_i, ε_F the Fermi energy or level, and k_B the Boltzmann constant. The temperature dependent charge density, $\rho(\mathbf{r},T)$, enters the self-consistency cycle by determining the effective potential, thereby the Hamiltonian, and thus the ϕ_i, i.e., $\phi_i = \phi_i[\rho(\mathbf{r},T)]$. The electronic free energy is given by

$$F^\mathrm{el}(T) = U^\mathrm{el}(T) - TS^\mathrm{el}(T), \tag{3}$$

with the internal energy $U^\mathrm{el}(T)$ often written as [38] $U^\mathrm{el}(T) = \sum_i f_i\,\varepsilon_i - E_\mathrm{dc}$, where $f_i = f(\varepsilon_i,T)$ and E_dc are double counting corrections, and with the configurational entropy

$$S^\mathrm{el}(T) = -\gamma k_B \sum_i [f_i \ln f_i + (1-f_i)\ln(1-f_i)], \tag{4}$$

where γ equals 1 for spin-polarized systems and 2 for spin-unpolarized systems. The above self-consistency procedure yields eigenvalues that, as the $\phi_i = \phi_i[\rho(\mathbf{r},T)]$, are implicitly depending on temperature, $\varepsilon_i = \varepsilon_i[\rho(\mathbf{r},T)]$, and therefore an implicitly temperature dependent electronic DOS:

$$D(\varepsilon)[\rho(\mathbf{r},T)] = \sum_i \delta(\varepsilon - \varepsilon_i[\rho(\mathbf{r},T)]). \tag{5}$$

B. Fixed density-of-states approximation

If one assumes that the electronic DOS is temperature independent, the electronic free energy can be approximately computed via Eq. (3) by utilizing the $T = 0\,\mathrm{K}$ electronic DOS, $D(\varepsilon) = D(\varepsilon)[\rho(\mathbf{r},T=0\,\mathrm{K})]$, as

$$\widetilde{F}^\mathrm{el}_\mathrm{DOS}(T) = \widetilde{U}^\mathrm{el}_\mathrm{DOS}(T) - T\widetilde{S}^\mathrm{el}_\mathrm{DOS}(T), \tag{6}$$

$$\widetilde{U}^\mathrm{el}_\mathrm{DOS}(T) = \int_{-\infty}^{\infty} D(\varepsilon)\,f\,\varepsilon\,\mathrm{d}\varepsilon - \int_{-\infty}^{\varepsilon_\mathrm{F}} D(\varepsilon)\,\varepsilon\,\mathrm{d}\varepsilon, \tag{7}$$

$$\widetilde{S}^\mathrm{el}_\mathrm{DOS}(T) = \gamma k_B \int_{-\infty}^{\infty} D(\varepsilon)\,s(\varepsilon,T)\,\mathrm{d}\varepsilon, \tag{8}$$

where

$$s(\varepsilon,T) = -[f\ln f + (1-f)\ln(1-f)] \tag{9}$$

and $f = f(\varepsilon,T)$ [Eq. (2)]. The tilde over the thermodynamic variables indicates the approximate evaluation. Note that in practical calculations often an artificial electronic temperature, such as for example in the Methfessel-Paxton scheme [39], is used to stabilize the electronic charge self-consistency when calculating $D(\varepsilon)[\rho(\mathbf{r},T=0\,\mathrm{K})]$.

C. Sommerfeld approximation

For low temperatures, the first integral of Eq. (7) can be expanded following the Sommerfeld expansion [40], yielding an even more simplified expression for the internal energy

$$\widetilde{U}^\mathrm{el}_\mathrm{SOM}(T) = \frac{\pi^2}{6}k_B^2T^2D(\varepsilon_\mathrm{F}) + O(T^4), \tag{10}$$

with the subscript "SOM" indicating the Sommerfeld approximation. The electronic entropy and free energy are then obtained from their fundamental thermodynamic relations to the internal energy [41]:

$$\widetilde{S}^\mathrm{el}_\mathrm{SOM}(T) = \int dT\,\frac{1}{T}\frac{\partial\widetilde{U}^\mathrm{el}_\mathrm{SOM}}{\partial T} = \frac{\pi^2}{3}k_B^2T\,D(\varepsilon_\mathrm{F}) + O(T^3), \tag{11}$$

$$\widetilde{F}^\mathrm{el}_\mathrm{SOM}(T) = -\frac{\pi^2}{6}k_B^2T^2D(\varepsilon_\mathrm{F}) + O(T^4). \tag{12}$$

The electronic contribution to the heat capacity (at constant volume), $\widetilde{C}^{\mathrm{el}}_{V,\mathrm{SOM}}$, can be computed as:

$$\widetilde{C}^{\mathrm{el}}_{V,\mathrm{SOM}}(T) = \frac{\partial \widetilde{U}^{\mathrm{el}}_{\mathrm{SOM}}}{\partial T} = \frac{\pi^2}{3} k_B^2 T D(\varepsilon_{\mathrm{F}}) + O(T^3). \quad (13)$$

D. Electronic free energies including lattice vibrations

The methodology discussed in Secs. II A to II C applies to a set of fixed atomic coordinates. A convenient choice are the ideal lattice sites (e.g., bcc, fcc, or hcp lattice) that correspond to the $T = 0$ K equilibrium positions of the atoms. Such an ideal lattice approximation yields the electronic free energy neglecting a possible impact of explicit thermal vibrations of the atoms.

To go beyond one needs to consider the electronic free energy derived from AIMD simulations. The formal background is provided by the free energy Born-Oppenheimer approximation [8,9], in which the atomic motion is determined adiabatically by the electronic free energy surface. For each AIMD snapshot, the electronic free energy, F^{el}_i, is calculated by the SCF procedure from Sec. II A and averaged according to

$$F^{\mathrm{el-vib}}(T) = \frac{1}{N} \sum_i^N \Delta F^{\mathrm{el}}_i(T), \quad (14)$$

with

$$\Delta F^{\mathrm{el}}_i(T) = F^{\mathrm{el}}_i(T) - U^{\mathrm{el}}_i(T = 0\,\mathrm{K}), \quad (15)$$

and i running over N AIMD snapshots representing a statistically converged thermal distribution at T. In Eq. (15), $U^{\mathrm{el}}_i(T = 0\,\mathrm{K})$ is the potential energy of snapshot i at an electronic temperature of $T = 0$ K. With this reference, $F^{\mathrm{el-vib}}$ gives the electronic free energy including the coupling to explicit vibrations, but excluding the potential energy of the lattice degrees of freedom. Note that, in principle, ΔF^{el}_i could be also computed using either the fixed DOS or Sommerfeld approximation (as done below in Sec. IV D for test purposes). However, since AIMD requires a self-consistency cycle in any case, these approximations are not computationally beneficial.

III. METHODOLOGICAL DETAILS

We used the projector augmented wave method [42] and the PBE functional [43] as implemented in VASP [44,45], in combination with the provided potentials [38]. For the early transition metals (up to Mn, Tc, and Re), the p states were treated as valence states [46]. For the ideal static lattice calculations, the plane-wave cutoff was set to twice the suggested maximum value, and the k-point meshes were set to $40 \times 40 \times 40$ for the 1-atom bcc and fcc cells (64 000 k-points · atom), and to $40 \times 40 \times 24$ for the 2-atom hcp cell (76 800 k-points · atom). For all the $T = 0$ K calculations, the tetrahedron method with Blöchl corrections [47] was used to improve the convergence with respect to the k-point sampling. For the hcp structure an ideal c/a ratio was used. For comparing the different levels of approximations, the volume was set to 1.08 times the equilibrium volume at $T = 0$ K, V_0, to approximately incorporate the thermal expansion at the temperatures of interest (1500 K and melting temperature). The actual dependence of the electronic excitations on the volume is discussed in Sec. IV A 2. We determined V_0 by fitting the Vinet equation [48] to at least 12 energy-volume points in a range of ±5% around V_0. Most of the calculations were performed without spin polarization to enable an interpretation of chemical trends. Bcc Fe, fcc Co, and fcc Ni were additionally computed in the ferromagnetic state to elucidate the impact of magnetism. In order to obtain a smooth DOS $D(\varepsilon)$ from the discrete set of computed eigenvalues ε_i for visualization purposes and for deriving the DOS at the Fermi level $D(\varepsilon_{\mathrm{F}})$ for the Sommerfeld approximation, we replaced the delta function in Eq. (5) by smooth Gaussian functions:

$$D(\varepsilon) = \frac{1}{\sigma\sqrt{\pi}} \sum_i \exp\left(- \frac{(\varepsilon - \varepsilon_i)^2}{\sigma^2} \right), \quad (16)$$

with the broadening/smearing parameter σ set generally to 0.1 eV. For the Sommerfeld approximation we also used $\sigma =$ 0.2 eV to test the influence on $D(\varepsilon_{\mathrm{F}})$.

For a subset of elements, namely bcc Nb, W; fcc Rh, Pt and hcp Re, Ru, we performed explicit AIMD simulations at different temperatures to investigate the impact of lattice vibrations. We used supercells with 54, 32, and 36 atoms for bcc, fcc, and hcp, respectively. Following the concept of the up-sampled thermodynamic integration using Langevin dynamics (UP-TILD) method [49], in a first step these calculations were performed based on relatively low DFT convergence parameters to provide an efficient but still accurate enough sampling of the configuration space. The cutoff energy was set to the default value of the potential from the VASP library and a $2 \times 2 \times 2$ k-point mesh was used (432, 256, 288 k-points · atom for bcc, fcc, hcp, respectively). The AIMD simulations were performed for about 5000 steps with a time step of 5 fs. The Langevin thermostat was used with a friction parameter of 0.01 fs^{-1}. In a following step, uncorrelated snapshots were extracted from the trajectories and recalculated with a denser k-point mesh ($8 \times 8 \times 8$; 27 648, 16 384, 18 432 k points · atom for bcc, fcc, hcp) to determine accurate electronic free energies for the averaging. For each element and at each temperature, ten uncorrelated snapshots extracted from well equilibrated AIMD simulations were sufficient for a statistical error below 1 meV/atom in Eq. (14). The reason for this is that each supercell in itself is the average over many distinct atomic sites.

IV. RESULTS AND DISCUSSION

A. SCF electronic free energies for ideal lattices

1. Temperature dependence

Figures 1(a)–1(c) show the electronic free energies for all investigated elements and structures with atoms on the ideal lattice sites at an electronic temperature of 1500 K, calculated self-consistently using Eq. (3), but referenced to the extrapolated internal energy at $T = 0$ K, i.e., showing $F^{\mathrm{el}} - U^{\mathrm{el}}$ ($T = 0$ K). For interpreting the observed trends, the fixed DOS approximation is helpful. From Eqs. (6)–(8) it is apparent that the electronic free energy is directly linked to the electronic DOS. In fact, a closer look reveals that only the DOS close to the Fermi level contributes to F^{el}. For the internal energy, this can be seen by considering that the first integral in Eq. (7) is canceled by the second one whenever

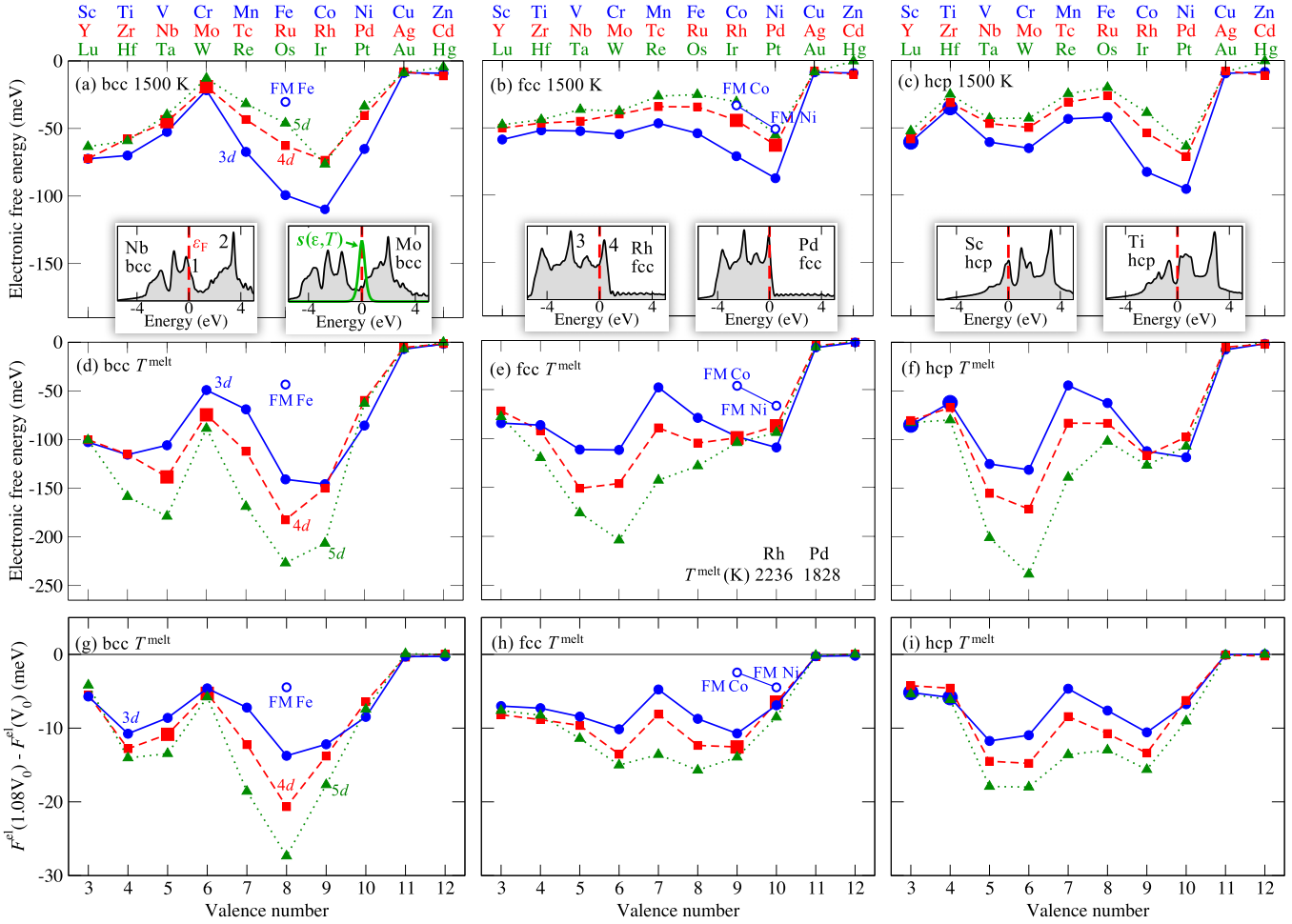

FIG. 1. Ideal lattice SCF electronic free energies in meV/atom at (a)–(c) 1500 K and (d)–(f) the respective melting points (T^{melt}, cf. Table II) referenced with respect to the internal energy at $T = 0$ K. (g)–(i) show the electronic free energy change upon a volume increase of 8% with respect to the equilibrium volume V_0. The insets in (a)–(c) show the electronic DOS (arbitrary units) for some of the elements (emphasized by slightly larger symbols in the respective plots) in the three different structures (bcc, fcc, hcp). The Fermi levels ε_F are indicated by the red dashed lines. For bcc Nb and fcc Rh, the numbers 1–4 indicate peaks that are relevant for the discussion in the text. For bcc Mo, the entropy distribution $s(\varepsilon, T = 1500\,\text{K})$ [Eq. (9)] is plotted (green line). Throughout the figure, results correspond to nonmagnetic calculations, except for the ferromagnetic (FM) results for bcc Fe, fcc Co, and fcc Ni (blue open circles). Exact numbers for all free energy values shown in (a)–(f) are given in Table II.

$f \approx 1$, i.e., at energies sufficiently below the Fermi level. For energies sufficiently above the Fermi level, i.e., $f \approx 0$, both integrals give a negligible contribution. Regarding the entropy, note that the function $s(\varepsilon, T)$ in Eq. (9) is only peaked around the Fermi level as exemplified by the green line in the inset of Fig. 1(a). The Sommerfeld approximation, Eq. (12), gives an even more specific relation between the electronic DOS and electronic free energy: A *large* DOS at the Fermi energy implies a *largely negative* free energy.

Consider the two examples shown in the insets of Fig. 1(a), bcc Nb and Mo. The DOS is higher at the Fermi level for bcc Nb than for bcc Mo yielding a more negative free energy at 1500 K for Nb: −47 vs Mo: −20 meV/atom [cf. large red squares in Fig. 1(a)]. For the subsequent 4*d* bcc elements [see Fig. 1(a)], the free energy decreases strongly to the right of Mo. This enhancement in magnitude is related to the peak in the DOS located above the Fermi level for Nb and Mo (marked with "2" in the Nb inset).

Indeed, according to the canonical *d* band model [30–32], the DOS does not significantly change across the *d* elements. We can therefore employ the DOS of Nb and Mo for statements about the other *d* elements. Increasing the number of valence electrons [i.e., going from left to right in Fig. 1(a)] only shifts the Fermi level to higher energies. The dependence of the electronic free energy for the bcc elements as a function of the *d* valence number hence reflects the peak structure of a generic bcc DOS. This applies to the 3*d*, 4*d*, and 5*d* transition elements, all having a very similar generic DOS and consequently a similar electronic free energy dependence [Fig. 1(a)].

The canonical *d* band model can similarly be used to correlate the dependence of the electronic free energy for the fcc and hcp elements with their generic DOS. As each geometry (bcc, fcc, hcp) leads to a different specific generic DOS [insets in Figs. 1(a)–1(c)], the corresponding electronic free energy trends [Figs. 1(a)–1(c)] likewise differ

TABLE II. Ideal lattice electronic free energies in meV/atom at 1500 K and at the indicated melting points ($T^{\rm melt}$ = experimental melting point in K from Ref. [50]) for all 3*d*, 4*d*, and 5*d* transition metals for the bcc, fcc, and hcp structures computed using the SCF approach, Eqs. (1)–(4). Values correspond to nonmagnetic calculations except for the ferromagnetic (FM) results for bcc Fe, fcc Co, and fcc Ni. The subscripts "sv" and "pv" indicate the inclusion of semicore *s* and *p* electrons into the valence of the employed potentials.

		bcc		fcc		hcp	
Element	$T^{\rm melt}$	1500 K	$T^{\rm melt}$	1500 K	$T^{\rm melt}$	1500 K	$T^{\rm melt}$
Sc_{sv}	1814	−72	−103	−59	−84	−61	−85
Ti_{pv}	1943	−70	−116	−52	−86	−35	−62
V_{pv}	2183	−53	−106	−52	−111	−61	−125
Cr_{pv}	2180	−22	−49	−55	−112	−65	−131
Mn_{pv}	1519	−67	−69	−47	−48	−43	−44
Fe	1811	−99	−141	−54	−79	−42	−63
Fe(FM)	1811	−30	−44				
Co	1768	−110	−146	−71	−98	−83	−112
Co(FM)	1768			−33	−46		
Ni	1728	−65	−86	−87	−109	−95	−118
Ni(FM)	1728			−51	−67		
Cu	1358	−9	−7	−9	−7	−9	−8
Zn	693	−9	−2	−9	−2	−8	−2
Y_{sv}	1795	−72	−100	−50	−72	−58	−81
Zr_{sv}	2127	−58	−115	−46	−92	−31	−67
Nb_{pv}	2750	−45	−138	−45	−151	−47	−155
Mo_{pv}	2895	−19	−75	−40	−146	−50	−171
Tc_{pv}	2430	−43	−112	−34	−89	−31	−83
Ru	2606	−63	−182	−34	−105	−26	−83
Rh	2236	−73	−150	−44	−99	−54	−116
Pd	1828	−40	−60	−63	−87	−71	−97
Ag	1235	−8	−5	−8	−5	−8	−5
Cd	594	−11	−2	−10	−1	−11	−2
Lu	1936	−63	−101	−48	−78	−52	−83
Hf_{pv}	2506	−59	−159	−44	−120	−25	−80
Ta_{pv}	3290	−40	−179	−36	−176	−43	−201
W_{sv}	3687	−13	−89	−38	−204	−43	−238
Re	3458	−32	−169	−26	−143	−25	−139
Os	3306	−46	−227	−25	−128	−20	−102
Ir	2719	−76	−207	−31	−104	−39	−126
Pt	2041	−34	−63	−55	−94	−64	−107
Au	1337	−9	−7	−8	−7	−8	−7
Hg	234	−5	0	0	0	0	0

from each other. (See Appendix for a compilation of all DOS'.)

The electronic free energy at a fixed absolute (electronic) temperature is, as just discussed, useful for analyzing the correlation to the DOS. When computing free energies one is, however, often interested in temperatures up to the respective melting point. The corresponding electronic free energies (still within the ideal lattice approximation) are shown in Figs. 1(d)–1(f). The dependencies clearly change with respect to those at a fixed absolute temperature, because of the strongly varying melting points across the *d* elements (see Table II). This is nicely illustrated for the example of Rh fcc and Pd fcc. At 1500 K, the relative magnitude of the free energy for Pd and Rh is determined exclusively by the DOS near the Fermi level, and hence the free energy of Pd has a magnitude 38% larger compared to Rh. At the respective (experimental) melting temperature, the trend reverses: Rh has a melting temperature of 2236 K [50], larger by 22% than that of Pd (1828 K [50]). As the free energy scales approximately quadratically with temperature, the temperature effect dominates and reverts the order of relative magnitudes.

Figures 1(d)–1(f) clearly show that the magnitude of the electronic free energy at the melting point can be significant, ≈ -250 meV/atom (bcc Os, $T^{\rm melt} = 3306$ K). Comparing the data for the same element but for different structures reveals that the magnitudes can be quite different, e.g., Ir bcc: −218, Ir fcc: −113, Ir hcp: −136 meV/atom. This highlights the importance of electronic contributions for determining phase stabilities and transition temperatures as the latter are known to strongly depend even on changes in the range of a few meV/atom in the free energy [25,51,52].

2. *Volume dependence*

Since at high temperatures, especially at the melting point, the volume change of the system can be significant, the impact of volume on the electronic free energy needs to be carefully addressed. In Figs. 1(g)–1(i) we show the change in the ideal lattice SCF electronic free energies at the melting point upon increasing the volume from the equilibrium volume at $T = 0$ K, V_0, to a volume of $1.08V_0$, which reflects a

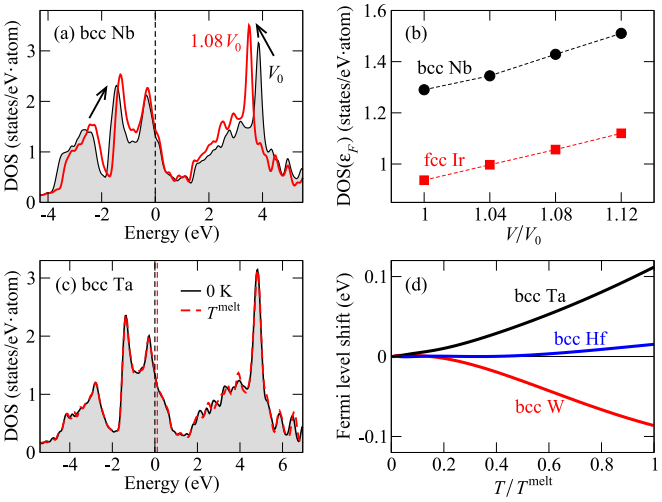

FIG. 2. Influence of volume and temperature on the electronic DOS. (a) Change of the DOS for bcc Nb upon increasing the volume from V_0 (equilibrium volume at $T = 0$ K, black line and gray shading) to $1.08V_0$ (red line). The resulting compression is emphasized by the arrows, and the Fermi level (the same for both DOS') is marked by the black dashed line. (b) Change of the DOS directly at the Fermi level, $\varepsilon_{\rm F}$, with volume for two examples. (c) Change of the DOS for bcc Ta upon increasing the (electronic) temperature from $T = 0$ K (black line and gray shading) to $T^{\rm melt} = 3290$ K (red dashed line) within the self-consistent finite temperature DFT calculation. The black and red dashed lines mark the respective Fermi levels, the red line for the $T^{\rm melt}$ calculation being shifted by about 0.1 eV with respect to the black one. (d) Fermi level shift with temperature for three examples showing different dependencies (positive, small, negative).

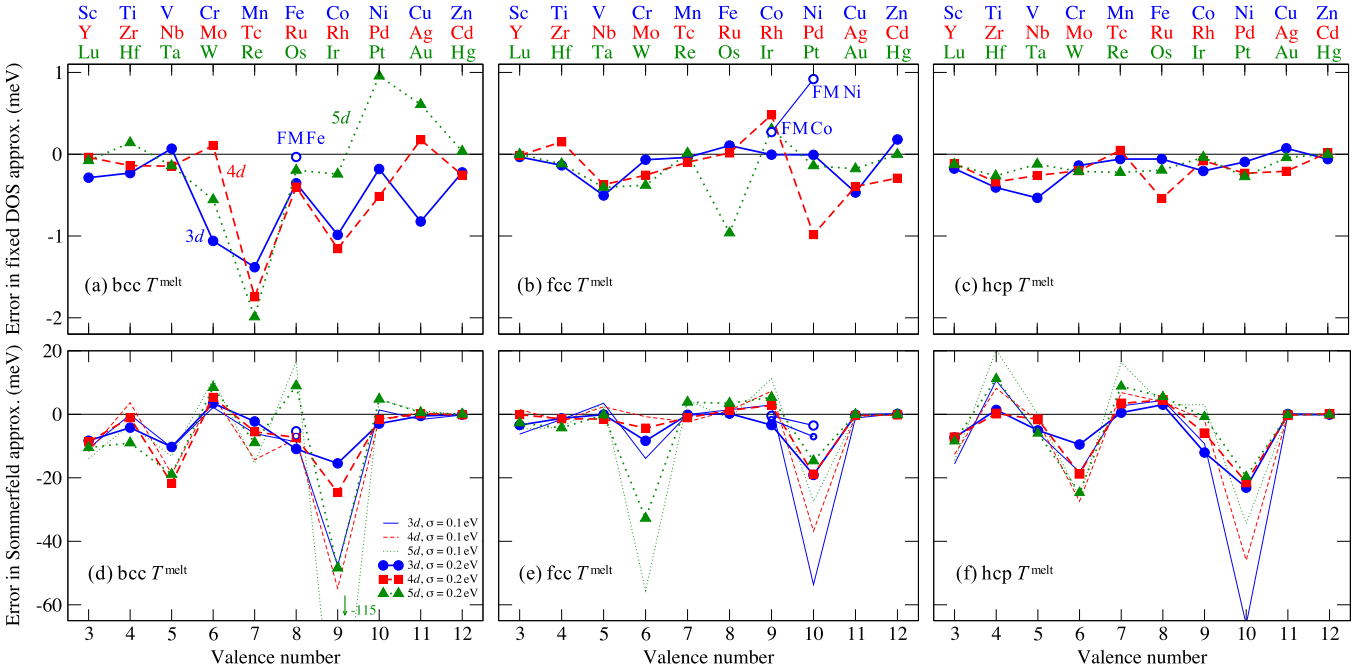

FIG. 3. (a)–(c) Error in the fixed DOS and (d)–(f) Sommerfeld approximation at an electronic temperature corresponding to the respective melting point T^{melt} for all $3d$ (blue dots), $4d$ (red squares), and $5d$ (green triangles) transition metals in the (a), (d) bcc, (b), (e) fcc, and (c), (f) hcp structures. The error is defined as the deviation from the SCF electronic free energy for an ideal lattice. In (d)–(f) the thick lines with symbols correspond to a smearing parameter $\sigma = 0.2$ eV and the thin lines without symbols to $\sigma = 0.1$ eV, used to obtain the corresponding DOS at the Fermi level. Throughout the figure, results correspond to nonmagnetic calculations, except for the data shown by the blue open circles which represent ferromagnetic (FM) calculations for bcc Fe, fcc Co, and fcc Ni.

reasonable estimate of the thermal expansion at the melting point. An important finding is that the electronic free energy decreases with increasing volume for all investigated elements. The overall magnitude of the free energy decrease due to the 8% volume change is for most of the investigated elements about 10% of the total electronic free energy [Figs. 1(d)–1(f)], and consequently the general chemical trends are similar.

The negative dependence of the electronic free energy on the volume can be understood by examining the variation of the electronic DOS with volume. As a representative example, the electronic DOS of bcc Nb is shown in Fig. 2(a) at V_0 (black line and gray shading) and $1.08V_0$ (red line). As the volume increases, the generic features of the electronic DOS do not change except for an overall compression of the d band (exemplified by the arrows), centered around the Fermi level. This compression is a consequence of the well-known reduction of d-band width as the d-orbital overlap decreases with increasing distance between the atoms. Since the Fermi level is determined by the conservation of the number of electrons, it remains in a similar relative position after the volume change, as compared, e.g., to the neighboring peak. Further, since the total spectral weight of the d band must remain the same the compression leads to an overall increase of the DOS, inversely proportional to the reduction in d-band width, as can be observed by comparing the heights of the peaks in Fig. 2(a). In consequence, increasing the volume leads to an increase of the DOS at the Fermi level [Fig. 2(b)] and hence to an increase in entropy and a corresponding lowering of the free energy.

B. Fixed density-of-states approximation

We now turn to the error introduced by the fixed DOS approximation [Eqs. (6)–(8)]. We focus on the deviation from the ideal lattice SCF electronic free energy at the melting point which can be considered as the most severe condition for the validation. As shown in Figs. 3(a)–3(c), for most of the elements the corresponding error is below 1 meV/atom. Only a few cases, e.g., bcc Tc and Re, show a slightly higher error, up to 2 meV/atom. The performance of this approximation is best for hcp structures, with errors of less than 0.5 meV/atom. Noting that all errors will decrease upon lowering the temperature, we can safely conclude that the fixed DOS approximation is in general an excellent approximation to calculate electronic free energies.

Compared with the SCF method, the fixed DOS approximation neglects the variation of the electronic DOS with temperature. The validity of this assumption is illustrated in Fig. 2(c) for bcc Ta, showing a comparison of the DOS at $T = 0$ K (black line) and at the melting temperature (red dashed line) using the identical volume. As the temperature is increased, the profile of the DOS remains almost the same (i.e., the red dashed curve and the black solid curve overlap) except for a shift of the Fermi energy (cf. distance between the vertical black and red lines). The Fermi energy shift, $\varepsilon_{\text{shift}}$, can be determined by

$$\int_{-\infty}^{\infty} D(\varepsilon)\, f(\varepsilon - \varepsilon_{\text{shift}}, T)\, \mathrm{d}\varepsilon = \int_{-\infty}^{\varepsilon_{\text{F}}} D(\varepsilon)\, \mathrm{d}\varepsilon = N_{\text{el}}, \quad (17)$$

which ensures the preservation of the total number of electrons, N_{el}. The shift will be small [bcc Hf in Fig. 2(d)] when the DOS can be expanded reasonably well in even functions around the Fermi level. In this case, excited electrons will be able to populate energy states symmetrically around the (original, $T = 0$ K) Fermi level. The shift will be larger [$\approx \pm 0.1$ eV; see bcc Ta and bcc W in Fig. 2(d)] for DOS' that are strongly deviating from an even description around the Fermi level, because then excited electrons will asymmetrically populate the empty energy states.

C. Sommerfeld approximation

The virtue of the Sommerfeld model is that it provides simple analytical formulas for the thermodynamic potentials [Eqs. (10)–(12)], which are for example important for parametrizations in thermodynamic modeling approaches (such as, e.g., the CALPHAD approach [53,54]). Since the Sommerfeld model is based on a low temperature expansion it is critical to know its performance up to the melting point. Figures 3(d)–3(f) show that the error in the electronic free energy caused by the Sommerfeld approximation can reach several tens of meV/atom at T^{melt}. An additional difficulty is that the error critically depends on the technical details of the DOS calculation. The value of the electronic DOS at the Fermi level, which solely determines the electronic free energy in the Sommerfeld model, can sensitively depend on the broadening (aka smearing) parameter used to derive a smooth DOS from the discrete set of eigenvalues [Eq. (16)]. As an example, errors for two different smearing parameters of 0.1 and 0.2 eV are shown in Figs. 3(d)–3(f) (thin and thick lines), indicating that a smaller error is generally associated with a larger smearing parameter. For a fixed smearing parameter, e.g., 0.2 eV, the magnitude of the error varies significantly across the d series, ranging from less than 1 meV (e.g., for bcc Zr, fcc V) to several tens of meV (e.g., for bcc Ir, fcc W) per atom.

It is useful to elucidate the origin of the deviations exhibited by the Sommerfeld model. For that purpose we compare in Fig. 4 the DOS of an element revealing a small error (1 meV/atom, fcc Ru) to an element revealing a large error (48 meV/atom, bcc Ir). One simplification within the Sommerfeld model is the assumption that the DOS close to the Fermi energy varies smoothly. It can be seen in Fig. 4(a) that the DOS of fcc Ru exhibits comparably small fluctuations close to the Fermi energy. The Fermi energy (vertical dashed line) is located close to a shallow valley where the DOS is not sensitive to the employed smearing parameter (cf. black solid line and blue dashed line). In contrast, as shown in Fig. 4(b), the DOS of bcc Ir has a sharp peak directly at the Fermi energy, the height of which changes strongly with the smearing parameter. The observation that the Sommerfeld approximation exhibits large and sensitive errors when the Fermi energy is located at a sharp DOS peak is general. The bcc elements with 5 (V, Nb,

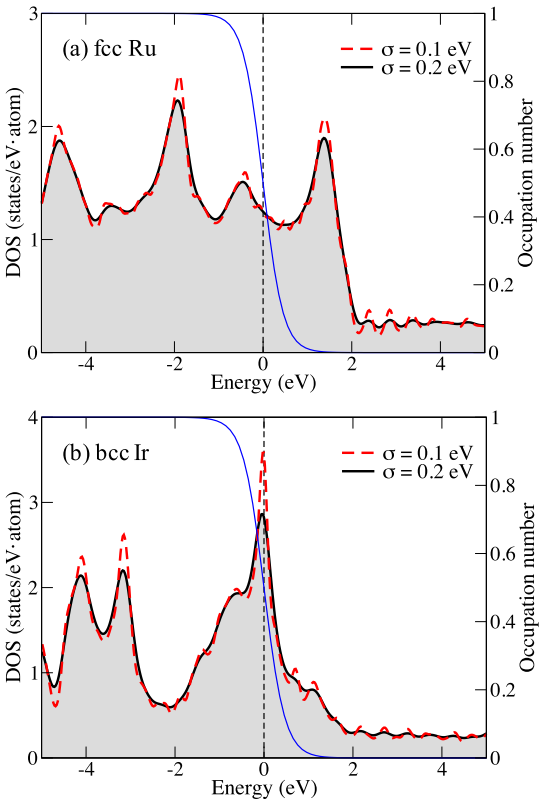

FIG. 4. Electronic DOS for (a) fcc Ru and (b) bcc Ir at $T = 0$ K, obtained with two different smearing parameters, σ, of 0.1 eV (red dashed lines) and 0.2 eV (black lines and gray shading) in Eq. (16). The blue solid lines indicate the Fermi-Dirac occupation function at the respective melting points (Ru: 2606 K and Ir: 2719 K).

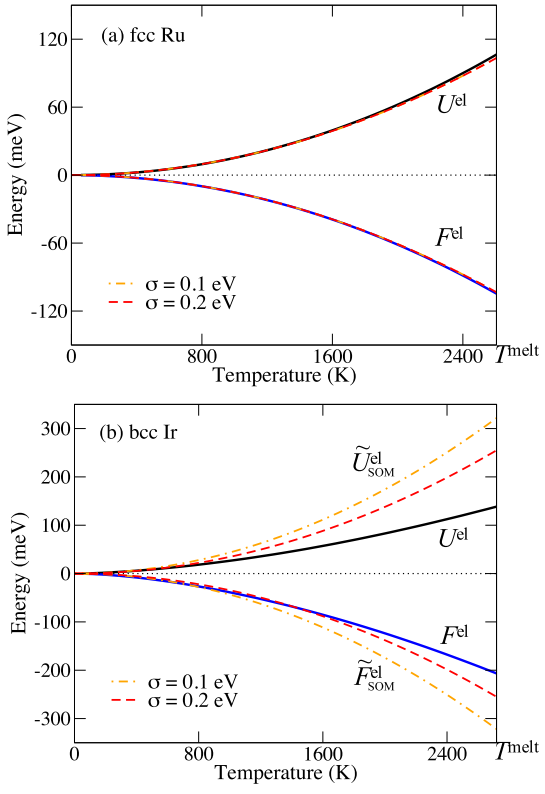

FIG. 5. Temperature dependence of the SCF electronic internal energy U^{el} (black lines) and the SCF electronic free energy F^{el} (blue lines) for (a) fcc Ru and (b) bcc Ir up to the respective melting points, T^{melt}. The red dashed lines and orange dash-dotted lines show results of the corresponding Sommerfeld approximation [Eqs. (10) and (12)] for two different smearing parameters ($\sigma = 0.1$ eV and $\sigma = 0.2$ eV).

and Ta) and 9 (Co, Rh, and Ir) valence electrons have large errors, because their Fermi level hits the peaks labeled 1 and 2 in the inset of Fig. 1(a). Similarly, the large errors for fcc Cr, Mo, and W are connected to the peak labeled 3 in the inset of Fig. 1(b) and the errors for fcc Ni, Pd, and Pt with the peak labeled 4.

A second simplification within the Sommerfeld model is the neglect of the higher-order terms in the expansions Eqs. (10)–(12). To elucidate the importance of these terms we plot in Fig. 5 the temperature dependence of the internal energy and free energy for fcc Ru and bcc Ir up to the respective T^{melt}. All solid lines have been calculated using the SCF procedure, i.e., using Eqs. (1)–(4) and performing a full self-consistency cycle at each temperature. Figure 5 also includes the results from the Sommerfeld approximation (dashed and dash-dotted lines), using Eqs. (10) and (12), and neglecting all but the lowest-order term ($\sim T^2$ term). For fcc Ru shown in Fig. 5(a), the Sommerfeld model nicely reproduces the SCF dependence even up to the melting point of 2606 K [50], revealing that the electronic internal energy and free energy of fcc Ru depend quadratically on temperature. However, fcc Ru is a rare case and many elements such as, e.g., bcc Ir reveal rather strong deviations from the quadratic dependence. In Fig. 5(b), the $\widetilde{U}^{\mathrm{el}}_{\mathrm{SOM}}$ curve (dashed line above zero) deviates significantly from the SCF U^{el} curve at about 30% of the melting point. The $\widetilde{F}^{\mathrm{el}}_{\mathrm{SOM}}$ curve (dashed line below zero) starts to deviate from F^{el} at about 10% of the melting point, with the error changing the sign. For most of the $3d$, $4d$, and $5d$ elements the assumption of a quadratic T dependence is thus not justified for an accurate determination of the electronic free energy.

D. Impact of explicit lattice vibrations

All results discussed so far have been obtained with the atoms placed on their ideal lattice sites. This assumption neglects the impact of atomic vibrations on the electronic free energy. Investigating the corresponding error requires expensive AIMD simulations and we therefore restricted our attention to a few representative elements: bcc Nb, W; fcc Rh, Pt; hcp Re, Ru. This choice represents elements in their experimentally observed, stable phases, it covers the three investigated lattices and also the $4d$ and $5d$ elements. See the study on Fe in Ref. [29] for an example of a $3d$ element.

Figure 6 shows the change in the electronic free energy upon including the thermal vibrations at the melting point, where the highest impact can be expected. The black bars correspond to our reference computed by the SCF procedure for an ideal lattice [more precisely $F^{\mathrm{el}} - U^{\mathrm{el}}$ ($T = 0$ K) as in Sec. IV A] and the red bars show the AIMD results including explicit vibrations according to Eq. (14). The changes induced by the atomic motion can be positive or negative, with a substantial magnitude ranging from a few meV/atom (e.g., fcc Rh: −4) to a few tens of meV/atom (e.g., bcc W: −50).

The observed behavior can be understood by analyzing the averaged electronic DOS' obtained from the AIMD

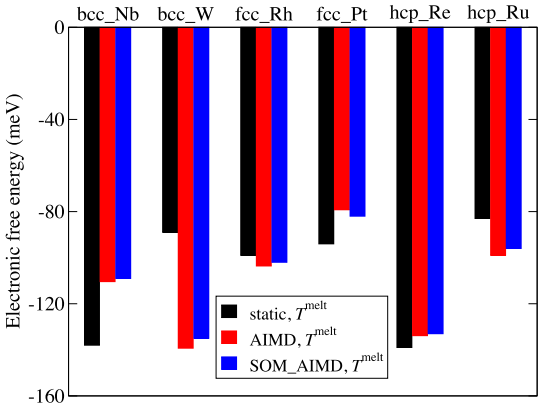

FIG. 6. Comparison of the electronic free energies in meV/atom extracted from AIMD simulations (red bars) with those computed via the SCF finite temperature DFT approach for an ideal static lattice (black bars). The blue bars correspond to the Sommerfeld approximation but using the effective DOS from the AIMD simulations as input.

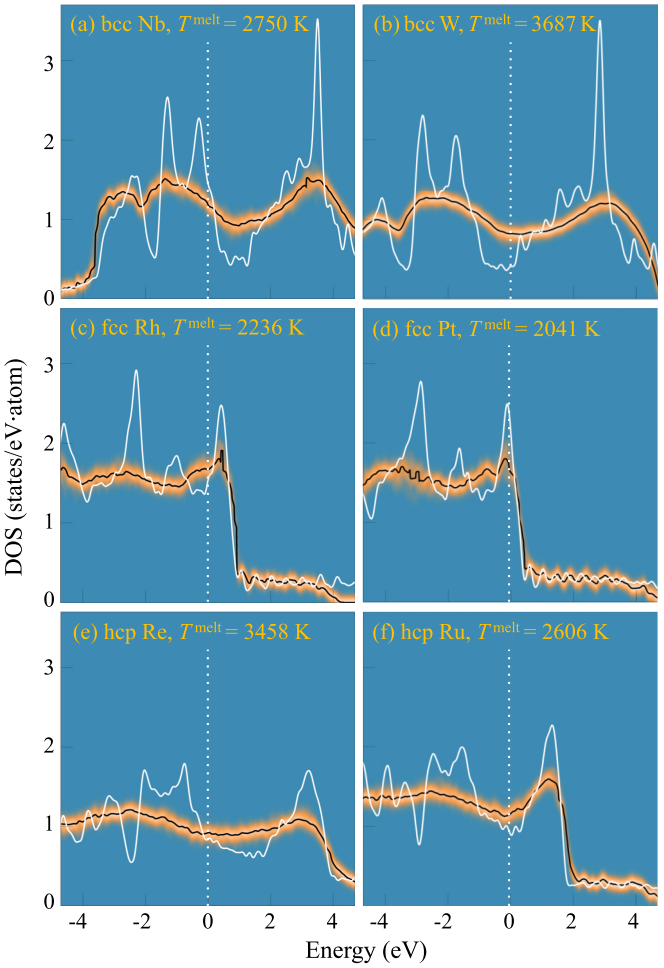

FIG. 7. Influence of lattice vibrations on the electronic DOS for a few selected elements at their respective melting temperatures, extracted from AIMD simulations. The black lines indicate the mean value from a statistically converged set of uncorrelated AIMD snapshots and the orange gradient shows the corresponding standard deviation. The white solid lines show the DOS obtained from static calculations for the ideal lattices at an electronic temperature corresponding to the melting point. The white dotted lines indicate the Fermi level.

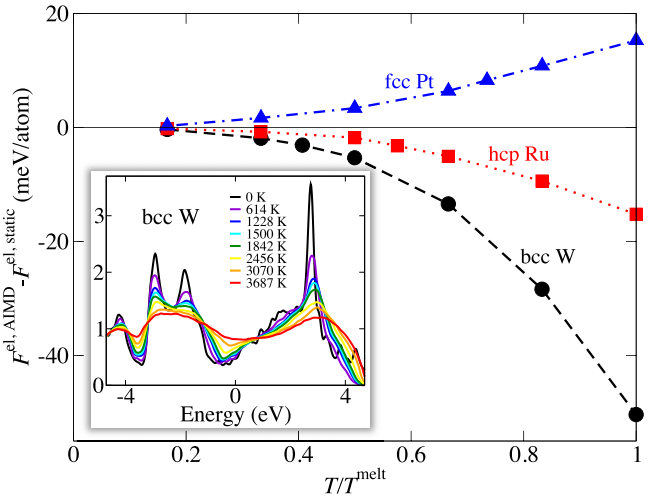

FIG. 8. Temperature dependence of the change in the electronic free energy due to thermal lattice vibrations for bcc W (black circles), fcc Pt (blue triangles), and hcp Ru (red squares). The temperature axis has been normalized by the respective melting temperature. The inset shows the temperature dependence of the effective electronic DOS (in units of states/eV · atom) for bcc W from the AIMD simulations.

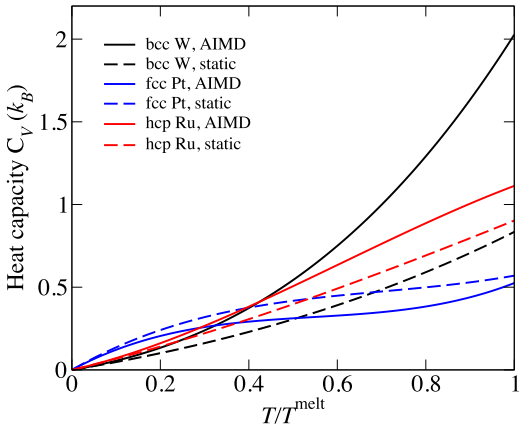

FIG. 10. Temperature dependence of the constant volume electronic heat capacity for bcc W (black), fcc Pt (blue), hcp Ru (red) with (solid lines) and without (dashed lines) the impact of vibrations. To obtain an accurate heat capacity from the coarse set of free energies (see Fig. 8), we used a physically motivated fit as introduced in Ref. [25] with a second-order polynomial for the energy independent electronic density of states. For consistency, the same fit was used to obtain the temperature dependence of the ideal lattice SCF heat capacities (dashed lines). The temperature axis has been normalized by the respective melting temperature.

simulations, as shown in Fig. 7 by the black solid lines. A significant broadening and smoothening is visible when compared to the $T = 0$ K electronic DOS' represented by the white solid curves. Sharp peaks are strongly smeared out and damped, and valleys are filled up with electronic states. These findings are consistent with previous studies for Mo [28] and Fe [29]. The reason for such a behavior is the loss of the crystal symmetry—a main ingredient to the pronounced peak profiles of the $T = 0$ K DOS'—induced by the thermal vibrations. The disordered atomic positions result in a much

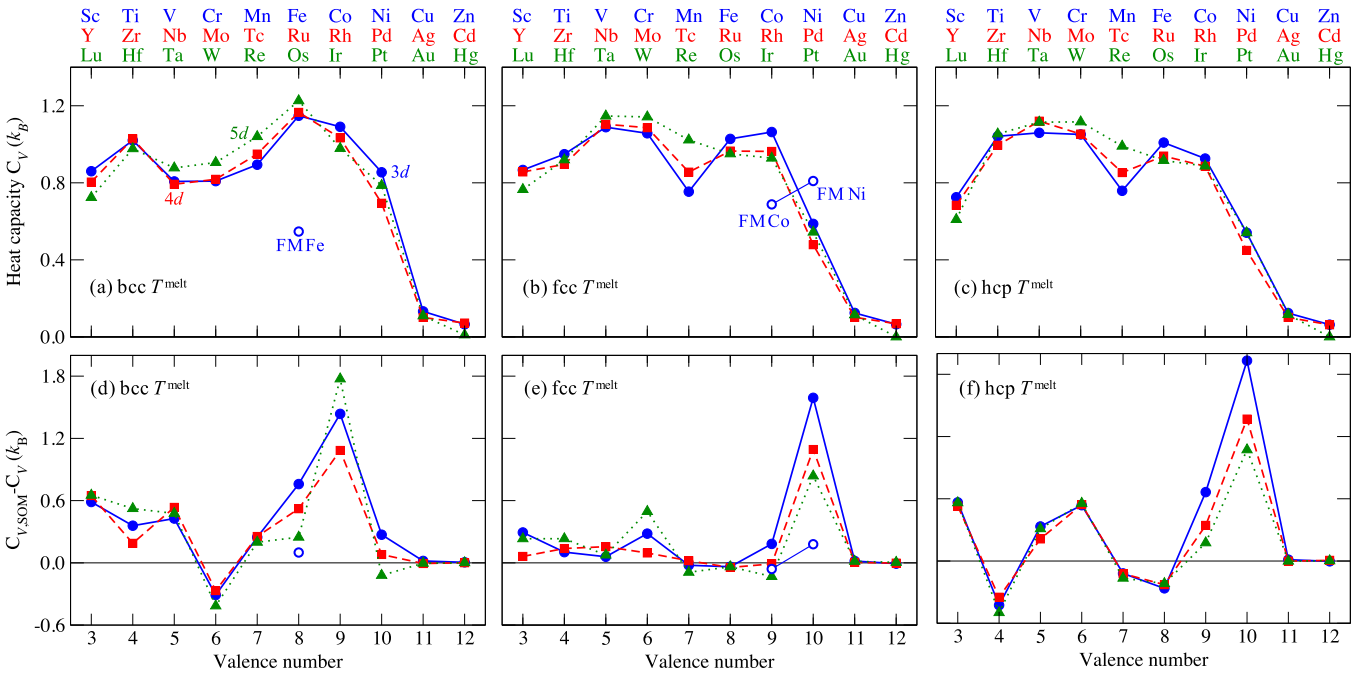

FIG. 9. (a)–(c) Ideal lattice SCF electronic contribution to the constant volume heat capacity and (d)–(f) error of the Sommerfeld approximation at the melting point (T^{melt}) and $1.08V_0$ for all 3d (blue dots), 4d (red squares), and 5d (green triangles) transition metals in the (a), (d) bcc, (b), (e) fcc, and (c), (f) hcp structures. The ideal lattice SCF heat capacity was obtained from a finite difference of the temperature dependence of the electronic internal energy (using 1 K steps). The Sommerfeld heat capacity was calculated with Eq. (13), using $\sigma = 0.1$ eV for smoothing the required DOS at the Fermi level. Throughout the figure, results correspond to nonmagnetic calculations, except for the data shown by the blue open circles which represent ferromagnetic (FM) calculations for bcc Fe, fcc Co, and fcc Ni.

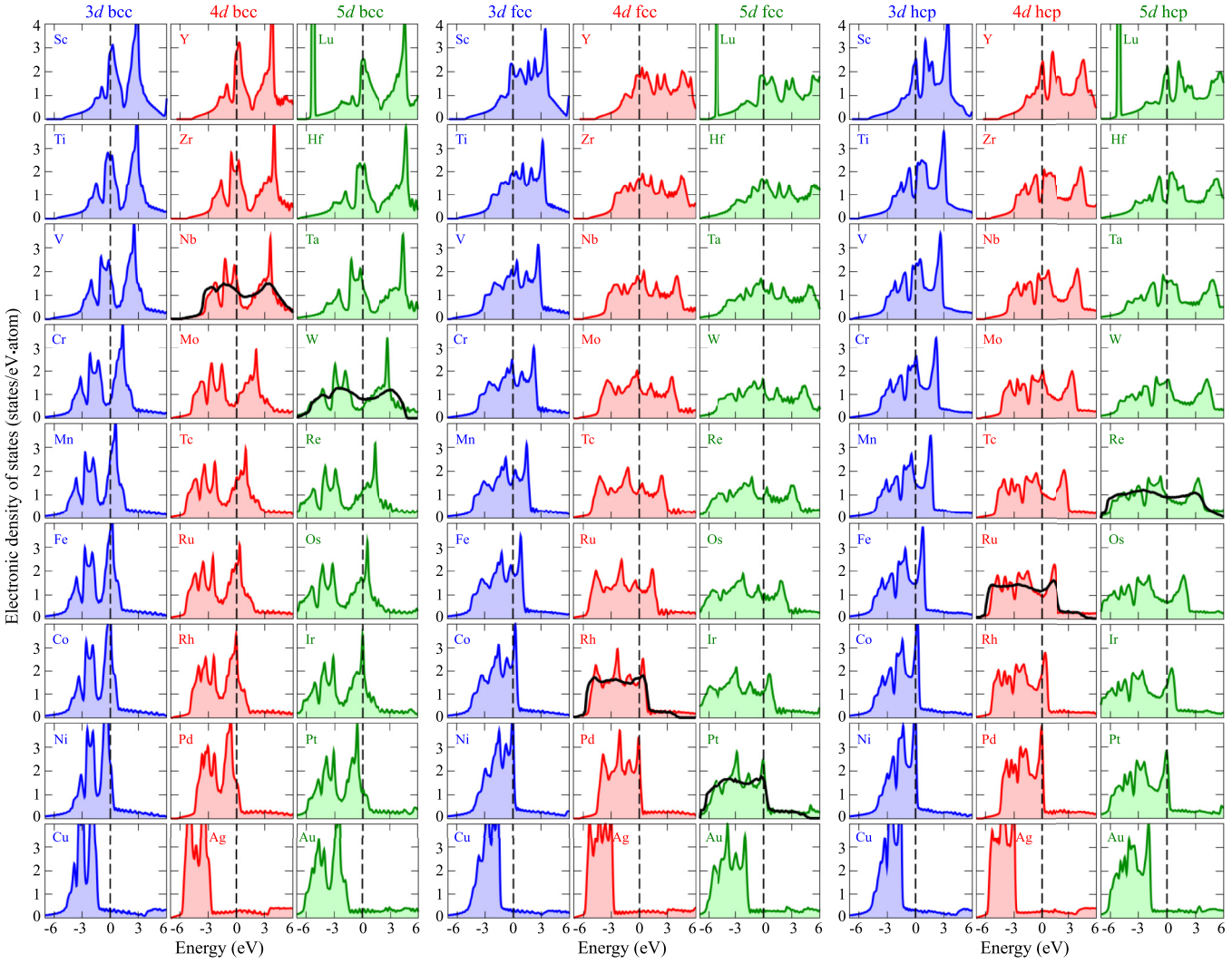

FIG. 11. Electronic densities of states for all 3*d* (blue), 4*d* (red), and 5*d* (green) elements on the ideal lattices of bcc, fcc, and hcp in the nonmagnetic state, and at an electronic temperature of $T = 0$ K and a volume of $1.08\,V_0$, referenced with respect to the Fermi level (marked by the vertical dashed lines). The shift due to an increase in the electronic temperature up to the melting point is negligible on the shown scale. The black solid lines show the effective mean DOS' from the AIMD simulations at the melting temperature for the investigated cases. All DOS' were obtained with a smoothing parameter of $\sigma = 0.1$ eV.

more homogeneous distribution of the energy levels compared to the perfect static lattice. The homogeneous distribution applies already to each single snapshot and the differences between the DOS' of (uncorrelated) snapshots are small as evidenced by the small standard deviation (orange gradient in Fig. 7). This finding suggests that the number of k points required to sample the Brillouin zone could be reduced for high temperature calculations. Future studies are required to quantify this statement.

The strong smoothening of the electronic DOS has a considerable effect on the electronic free energy, in full analogy to the discussions of the previous sections. Whenever the Fermi level is located close to a sharp peak in the original $T = 0$ K electronic DOS, as for bcc Nb, the damping of the peak leads to a reduction of the effective DOS at the Fermi level and consequently to a reduction of the magnitude of the electronic free energy. When the Fermi level is located inside a valley of the original $T = 0$ K electronic DOS, as for bcc W, the broadening leads to an increase of the effective DOS at the Fermi level and of the magnitude of the electronic free energy. An interesting side effect of the thermal broadening is an increase in the accuracy of the Sommerfeld model, provided one employs the high temperature effective DOS as input. The differences with respect to the full AIMD based electronic free energy are in the range of a few meV/atom (blue vs red bars in Fig. 6).

We have also investigated the temperature dependence of the impact of thermal vibrations on the electronic free energy. Figure 8 shows respective results for bcc W, fcc Pt, and hcp Ru. A nonlinear temperature dependence can be observed for all three elements. The changes in the electronic free energy can be again traced back to the broadening of the electronic DOS with temperature as exemplified for bcc W in the inset. The exact type of the temperature dependence of the electronic free energy is difficult to deduce, but it is conceivable that a linear dependence is unlikely to occur due to the complex changes in the electronic DOS with temperature.

E. Electronic contribution to the heat capacity

As one of the key thermodynamic properties, heat capacities can be either measured experimentally or calculated theoretically. They are an important ingredient to thermodynamic modeling approaches of phase stabilities and phase diagrams, such as the CALPHAD approach [53,54]. For such a modeling it is useful to have a good estimate of the magnitude and of the temperature dependence of the different heat capacity contributions. For low temperatures, it is well known that the electronic heat capacity contribution depends linearly on temperature as can be derived from the Sommerfeld model [cf. Eq. (13)] [16,20,23,55]. We focus here on the electronic heat capacity at high temperatures.

Figures 9(a)–9(c) show the electronic heat capacities calculated by the SCF method for all investigated elements at the respective melting temperatures within the ideal, static lattice approximation. The magnitude of the electronic heat capacities is in the order of $\sim 1\ k_B$ with the exception of the late transition elements (valence numbers 11 and 12). A contribution of $\sim 1\ k_B$ is significant and is also in the order of other contributions (e.g., due to thermal expansion or anharmonic vibrations [7]). In fact, one should note that the electronic contribution to the heat capacity at constant pressure, which corresponds to the typical experimental conditions, will be 30% larger than the here considered contribution to the constant volume heat capacity [56].

The fixed DOS approximation provides very accurate electronic heat capacities (not shown) with a maximum error of 0.03 k_B and most of the errors well below 0.01 k_B. One should be however cautious when using the linear Sommerfeld extrapolation up to the melting temperature. From Figs. 9(d)–9(f) it is apparent that the corresponding errors can be significant, mostly overestimating the SCF heat capacity values. The maximum deviation can even reach up to a factor of 2 of the corresponding absolute value (e.g., fcc Ni). The critical cases are characterized by sharp peaks or dips in the DOS near the Fermi level.

Another source of error is the ideal lattice approximation, similarly as for the electronic free energies. The importance of lattice vibrations on the electronic heat capacity is shown in Fig. 10 for three representative elements bcc W, fcc Pt and hcp Ru. Dashed lines represent the electronic heat capacity from the SCF procedure for the ideal lattices and solid lines the AIMD computed heat capacities. For fcc Pt and hcp Ru the impact of lattice vibrations is comparably small. In contrast, bcc W shows a strong impact with more than a factor of two increase arising from the vibrations at the melting point. This behavior can be traced back to the significant nonlinear temperature dependence of the electronic free energy including lattice vibrations (Fig. 8).

V. CONCLUSIONS

By conducting a wide-range investigation for all *d* transition elements for various ideal, static crystal lattices using finite temperature density-functional-theory calculations, we have systematically quantified general chemical trends of the electronic free energy and its relation to the electronic density of states. In agreement with previous knowledge, a high electronic density of states close to the Fermi energy results in a significant, negative electronic free energy contribution, in qualitative agreement with the Sommerfeld prediction. The dependence of the electronic free energy on the valence number therefore reflects the shape of a generic density of states, determined by the geometry of the crystal structure (bcc, fcc, hcp). The magnitude of the calculated electronic free energies as well as electronic heat capacities at high temperatures highlights the importance of electronic contributions in determining phase stabilities and phase diagrams.

Using this set of data and additional *ab initio* molecular dynamics simulations for selected cases allowed us to quantitatively assess the performance of three widely used approximations for computing electronic free energies. (1) The fixed density of states approximation, which neglects the temperature dependence of the density of states, performs extremely well for all investigated elements and structures, with errors in the electronic free energy of mostly below 1 meV/atom at the melting point. Electronic

TABLE III. Electronic densities of states at the Fermi level in states/eV · atom for all investigated elements and structures in the nonmagnetic state at a volume of $1.08V_0$. The first row for each element shows the DOS for the ideal static lattice at an electronic temperature of $T = 0$ K and the second row at an electronic temperature corresponding to the respective melting point. For a few selected elements and phases, the third row indicates the effective DOS at the Fermi level including the impact of thermal vibrations at the melting point. The subscripts "sv" and "pv" indicate the inclusion of semicore *s* and *p* electrons into the valence of the employed potentials.

3*d*	bcc	fcc	hcp	4*d*	bcc	fcc	hcp	5*d*	bcc	fcc	hcp
Sc_{sv}	2.8	2.3	2.5	Y_{sv}	2.9	1.8	2.4	Lu	2.5	1.8	2.1
	2.8	2.2	2.5		2.8	1.8	2.4		2.5	1.8	2.1
Ti_{pv}	2.5	1.9	1.1	Zr_{sv}	2.0	1.7	1.1	Hf_{pv}	2.1	1.6	0.8
	2.5	1.9	0.9		2.0	1.7	0.8		2.1	1.6	0.7
V_{pv}	2.0	1.9	2.3	Nb_{pv}	1.7	1.6	1.7	Ta_{pv}	1.5	1.3	1.5
	1.8	1.8	2.2		1.4	1.6	1.7		1.2	1.3	1.5
					1.2						
Cr_{pv}	0.8	2.2	2.6	Mo_{pv}	0.7	1.4	1.9	W_{sv}	0.5	1.6	1.6
	0.6	1.9	2.6		0.6	1.3	1.9		0.4	1.3	1.6
									0.8		
Mn_{pv}	2.7	1.7	1.5	Tc_{pv}	1.7	1.3	1.1	Re	1.3	1.0	0.8
	2.4	1.7	1.5		1.5	1.3	1.0		1.0	0.9	0.8
											0.9
Fe	3.7	1.9	1.5	Ru	2.3	1.2	1.0	Os	1.6	1.0	0.7
	3.6	1.9	1.4		2.3	1.2	0.9		1.6	0.8	0.7
							1.1				
Co	5.0	2.5	3.2	Rh	3.3	1.5	1.9	Ir	3.6	1.0	1.4
	3.9	2.4	2.9		2.2	1.5	1.8		3.2	1.1	1.3
						1.7					
Ni	2.3	4.4	5.0	Pd	1.5	3.0	3.5	Pt	1.2	2.4	2.8
	2.2	3.0	2.8		1.5	2.0	2.3		1.2	2.1	2.6
										1.6	
Cu	0.4	0.4	0.4	Ag	0.3	0.3	0.3	Au	0.3	0.3	0.3
	0.3	0.3	0.4		0.3	0.3	0.3		0.3	0.3	0.3
Zn	0.4	0.3	0.3	Cd	0.4	0.4	0.4	Hg	0.2	0.1	0.0
	0.3	0.3	0.3		0.4	0.3	0.4		0.2	0.0	0.0

heat capacities are likewise very well predicted. (2) The Sommerfeld approximation—when fed with the electronic density of states computed for the ideal static lattice—makes much more drastic assumptions and thus the corresponding error at high temperatures is about an order of magnitude larger. (3) The ideal lattice approximation neglects the impact of thermal atomic vibrations. The latter have a significant smoothening effect on the electronic density of states, and the resulting thermally averaged electronic free energy can change with respect to the ideal lattice electronic free energy by several tens of meV/atom. The details of these changes depend on the original location of the Fermi level with respect to peaks and valleys in the ideal, static electronic density of states.

Interestingly, the accuracy of the Sommerfeld approximation increases substantially when the effective electronic density of states from the molecular dynamics simulations is employed as input. Such an effective Sommerfeld model offers an interesting possibility for relatively simple but accurate parametrizations of the electronic free energy *including* the impact of thermal vibrations for CALPHAD based phase diagram approaches.

The smoothening of the effective electronic density of states by the thermal vibrations destroys the crystal structure specific peak profile inherent to the ideal static lattice density of states. The thermal disorder thus drives the electronic density of states towards a generic profile, weakly dependent on the crystal structure. We have shown this for a few selected elements but we believe that this holds for all *d* transition elements. We expect the insights and results of our study to be an important step towards the development of high accuracy databases of *ab initio* free energies for metals.

ACKNOWLEDGMENTS

We thank Professor Marcel H.F. Sluiter for fruitful discussions. Funding by the Deutsche Forschungsgemeinschaft (DFG) within the scholarship KO 5080/1-1 as well as by the European Research Council (ERC) under the European Union's Horizon 2020 research and innovation programme (Grant agreement No. 639211) is gratefully acknowledged.

APPENDIX: ELECTRONIC DENSITIES OF STATES

The complete set of the computed nonmagnetic densities of states is shown in Fig. 11. The corresponding DOS values at the Fermi level are given in Table III.

[1] G. Grimvall, B. Magyari-Köpe, V. Ozoliņš, and K. A. Persson, Rev. Mod. Phys. **84**, 945 (2012).
[2] O. Hellman, P. Steneteg, I. A. Abrikosov, and S. I. Simak, Phys. Rev. B **87**, 104111 (2013).
[3] M. Pozzo and D. Alfè, Phys. Rev. B **88**, 024111 (2013).
[4] C. Freysoldt, B. Grabowski, T. Hickel, J. Neugebauer, G. Kresse, A. Janotti, and C. G. Van de Walle, Rev. Mod. Phys. **86**, 253 (2014).
[5] M. Palumbo, B. Burton, A. C. E. Silva, B. Fultz, B. Grabowski, G. Grimvall, B. Hallstedt, O. Hellman, B. Lindahl, A. Schneider, P. E. A. Turchi, and W. Xiong, Phys. Status Solidi B **251**, 14 (2014).
[6] F. Körmann, A. A. H. Breidi, S. L. Dudarev, N. Dupin, G. Ghosh, T. Hickel, P. Korzhavyi, J. A. Muñoz, and I. Ohnuma, Phys. Status Solidi B **251**, 53 (2014).
[7] A. Glensk, B. Grabowski, T. Hickel, and J. Neugebauer, Phys. Rev. Lett. **114**, 195901 (2015).
[8] J. Cao and B. J. Berne, J. Chem. Phys. **99**, 2902 (1993).
[9] B. Grabowski, T. Hickel, and J. Neugebauer, Phys. Status Solidi B **248**, 1295 (2011).
[10] C. Wolverton and A. Zunger, Phys. Rev. B **52**, 8813 (1995).
[11] D. A. Boness, J. Brown, and A. McMahan, Phys. Earth Planet. Inter. **42**, 227 (1986).
[12] E. Wasserman, L. Stixrude, and R. E. Cohen, Phys. Rev. B **53**, 8296 (1996).
[13] E. G. Moroni, G. Grimvall, and T. Jarlborg, Phys. Rev. Lett. **76**, 2758 (1996).
[14] C. Wälti, E. Felder, M. A. Chernikov, H. R. Ott, M. de Boissieu, and C. Janot, Phys. Rev. B **57**, 10504 (1998).
[15] B. Sadigh and V. Ozoliņš, Phys. Rev. B **57**, 2793 (1998).
[16] M. E. Manley, R. J. McQueeney, B. Fultz, R. Osborn, G. H. Kwei, and P. D. Bogdanoff, Phys. Rev. B **65**, 144111 (2002).
[17] Y. Wang, Z.-K. Liu, and L.-Q. Chen, Acta Materialia **52**, 2665 (2004).
[18] R. Arroyave, D. Shin, and Z.-K. Liu, Acta Materialia **53**, 1809 (2005).
[19] H. Y. Geng, M. H. F. Sluiter, and N. X. Chen, J. Chem. Phys. **122**, 214706 (2005).
[20] R. Lortz, Y. Wang, U. Tutsch, S. Abe, C. Meingast, P. Popovich, W. Knafo, N. Shitsevalova, Y. B. Paderno, and A. Junod, Phys. Rev. B **73**, 024512 (2006).
[21] B. Grabowski, T. Hickel, and J. Neugebauer, Phys. Rev. B **76**, 024309 (2007).
[22] P. Souvatzis, O. Eriksson, and M. I. Katsnelson, Phys. Rev. Lett. **99**, 015901 (2007).
[23] Z. Lin, L. V. Zhigilei, and V. Celli, Phys. Rev. B **77**, 075133 (2008).
[24] Y. Wang, J. J. Wang, H. Zhang, V. R. Manga, S. L. Shang, L.-Q. Chen, and Z.-K. Liu, J. Phys.: Condens. Matter **22**, 225404 (2010).
[25] B. Grabowski, P. Söderlind, T. Hickel, and J. Neugebauer, Phys. Rev. B **84**, 214107 (2011).
[26] B. Kollmitzer and P. Hadley, Physica B **406**, 4373 (2011).
[27] M. Widom, in *High-Entropy Alloys: Fundamentals and Applications*, edited by C. M. Gao, J.-W. Yeh, K. P. Liaw, and Y. Zhang (Springer International Publishing, Cham, 2016), pp. 267–298.
[28] C. Asker, A. B. Belonoshko, A. S. Mikhaylushkin, and I. A. Abrikosov, Phys. Rev. B **77**, 220102(R) (2008).
[29] B. Alling, F. Körmann, B. Grabowski, A. Glensk, I. A. Abrikosov, and J. Neugebauer, Phys. Rev. B **93**, 224411 (2016).
[30] O. K. Andersen, Phys. Rev. B **12**, 3060 (1975).
[31] J. Madsen, O. K. Andersen, U. K. Poulsen, and O. Jepsen, AIP Conf. Proc. **29**, 327 (1976).
[32] D. G. Pettifor, J. Phys. F: Met. Phys. **7**, 613 (1977).

[33] N. D. Mermin, Phys. Rev. **137**, A1441 (1965).
[34] P. Hohenberg and W. Kohn, Phys. Rev. **136**, B864 (1964).
[35] S. Pittalis, C. R. Proetto, A. Floris, A. Sanna, C. Bersier, K. Burke, and E. K. U. Gross, Phys. Rev. Lett. **107**, 163001 (2011).
[36] F. Körmann, A. Dick, B. Grabowski, B. Hallstedt, T. Hickel, and J. Neugebauer, Phys. Rev. B **78**, 033102 (2008).
[37] W. Kohn and L. J. Sham, Phys. Rev. **140**, A1133 (1965).
[38] G. Kresse and D. Joubert, Phys. Rev. B **59**, 1758 (1999).
[39] M. Methfessel and A. T. Paxton, Phys. Rev. B **40**, 3616 (1989).
[40] N. W. Ashcroft and N. D. Mermin, in *Solid State Physics*, 1st ed. (Harcourt College Publishers, Orlando, 1976), Chap. 2, pp. 29–56.
[41] D. C. Wallace, *Thermodynamics of Crystals* (Dover, New York, 1998).
[42] P. E. Blöchl, Phys. Rev. B **50**, 17953 (1994).
[43] J. P. Perdew, K. Burke, and M. Ernzerhof, Phys. Rev. Lett. **77**, 3865 (1996).
[44] G. Kresse and J. Furthmüller, Phys. Rev. B **54**, 11169 (1996).
[45] G. Kresse and J. Furthmüller, Comput. Mater. Sci. **6**, 15 (1996).
[46] For W, *s* and *p* states were treated as valence states since the W_{pv} potential suffered from ghost states at higher energies.
[47] P. E. Blöchl, O. Jepsen, and O. K. Andersen, Phys. Rev. B **49**, 16223 (1994).
[48] P. Vinet, J. Ferrante, J. H. Rose, and J. R. Smith, J. Geophys. Res. [Solid Earth Planets] **92**, 9319 (1987).
[49] B. Grabowski, L. Ismer, T. Hickel, and J. Neugebauer, Phys. Rev. B **79**, 134106 (2009).
[50] W. M. Haynes, *CRC Handbook of Chemistry and Physics* (CRC Press, Taylor & Francis Group, Boca Raton, 2015).
[51] C. Engin and H. M. Urbassek, Comp. Mater. Sci. **41**, 297 (2008).
[52] F. Körmann, T. Hickel, and J. Neugebauer, Curr. Opin. Solid State Mater. Sci. **20**, 77 (2016).
[53] L. Kaufman and H. Bernstein, *Computer Calculation of Phase Diagrams* (Academic Press, New York, 1970).
[54] N. Saunders and A. P. Miodownik, *Calphad (Calculation of Phase Diagrams): A Comprehensive Guide* (Pergamon, Oxford, 1998).
[55] C. Kittel, in *Introduction to Solid State Physics*, 8th ed. (Wiley, New Jersey, 2004), Chap. 6, p. 145.
[56] T. Hickel, B. Grabowski, F. Körmann, and J. Neugebauer, J. Phys.: Condens. Matter **24**, 053202 (2012).